Available online at www.sciencedirect.com
ScienceDirect
International Journal of Heat and Mass Transfer 51 (2008) 3825–3839
International Journal of HEAT and MASS TRANSFER
www.elsevier.com/locate/ijhmt

Single-phase and two-phase cooling using hybrid micro-channel/slot-jet module

Myung Ki Sung, Issam Mudawar *

Boiling and Two-Phase Flow Laboratory (BTPFL), Purdue University International Electronic Cooling Alliance (PUIECA), Mechanical Engineering Building, 585 Purdue Mall, West Lafayette, IN 47907-2088, USA

Received 16 August 2007; received in revised form 19 December 2007
Available online 20 March 2008

Abstract

This paper explores the single-phase and two-phase cooling performance of a hybrid micro-channel/slot-jet module using HFE-7100 as working fluid. Three-dimensional numerical simulation using the k–ε turbulent model is used to both assess the single-phase performance and seek a geometry that enhances heat removal capability and surface temperature uniformity while decreasing mean surface temperature. This geometry is then tested experimentally to validate the numerical findings and aid in the development of correlations for both the single-phase and two-phase heat transfer coefficients. The hybrid module is shown to maintain surface temperature gradients below 2 °C for heat fluxes up to 50 W/cm^2. Even without phase change, the hybrid module is capable of dissipating heat fluxes as high as 305.9 W/cm^2. Highly accurate single-phase correlations are developed using a superpositioning technique that consists of assigning a different heat transfer coefficient for each portion of the heat transfer area based on the dominant heat transfer mechanism for that portion. Increasing subcooling and/or flow rate is shown to delay the onset of nucleate boiling to a higher heat flux and higher surface temperature, as well as enhance critical heat flux (CHF). A correlation previously developed for hybrid micro-channel/micro-circular-jet module is deemed equally effective at predicting two-phase heat transfer data for the present hybrid module.

1. Introduction

The quest for cooling solutions in the electronics industry has identified few cooling schemes that can tackle the high heat fluxes anticipated for future high-performance devices. Key among those schemes are micro-channel flow and jet impingement [1]. Micro-channel heat sinks have the capacity to dissipate very large heat fluxes from small areas, are compact, and require small coolant inventory. Jet-impingement cooling combines several favorable attributes, including the capacity to dissipate very large heat fluxes and small pressure drop compared to micro-channel heat sinks.

Many published experimental works prove the effectiveness of micro-channel flow. For example, Tuckerman and Pease [2] demonstrated heat removal rates up to 790 W/cm^2 using water as working fluid. Bowers and Mudawar [3] achieved single-phase and two-phase heat fluxes as high as 3000 and 27,000 W/cm^2, respectively, with water flow in micro-tubes. Lelea et al. [4] investigated single-phase heat transfer of water in stainless steel micro-tubes. They showed conventional macro-channel correlations are applicable to single-phase water flow in micro-tubes with diameters as small as 0.1 mm. Other studies have been focused on numerical modeling of fluid flow and heat transfer in micro-channel heat sinks [5–8]. Qu and Mudawar [6] proved that the conventional Navier–Stokes and energy equations provide accurate predictions of a heat sink's single-phase performance. A significant portion of the recent literature on micro-channel heat sinks concerns two-phase behavior. The performance of a two-phase micro-channel heat sink is vastly superior to its single-phase counterpart. This performance enhancement is the result of significantly higher convective heat transfer coefficients, better axial temperature uniformity, reduced coolant flow rate

* Corresponding author. Tel.: +1 765 494 5705; fax: +1 765 494 0539.
E-mail address: mudawar@ecn.purdue.edu (I. Mudawar).

0017-9310/$ - see front matter © 2008 Elsevier Ltd. All rights reserved.
doi:10.1016/j.ijheatmasstransfer.2007.12.015

Nomenclature

a	empirical constant
A_t	area of copper block's top test surface
b	empirical constant
C	empirical constant
C_1, C_2, C_3	empirical constants
C_1, C_2, C_μ	turbulence model constants
c_p	specific heat at constant pressure
d_h	hydraulic diameter of channel
G	production of turbulent energy
h	two-phase convective heat transfer coefficient, $q''_{eff}/(T_s - T_{in})$
H	height of unit cell
H_{ch}	height of channel
H_{jet}	height of jet
H_{th}	height from unit cell bottom boundary to thermocouple holes
H_w	height from unit cell bottom boundary to test surface
k	thermal conductivity; turbulent kinetic energy
L	length of unit cell (also length of micro-channel)
L_{jet}	length of slot jet
L_1, L_2, L_3, L_4	distance between thermocouple holes
n	empirical constant
Nu	Nusselt number
P	pressure
p_h	perimeter of micro-channel
Pr	Prandtl number
Pr_t	turbulent Prandtl number
P_W	electrical power supplied to copper heating block
q''	heat flux
q''_{eff}	effective heat flux based on top test surface area of copper block, $q''_{eff} = P_W/A_t$
Re_{jet}	jet Reynolds number, $Re_{jet} = \rho_f U_{jet}(2W_{jet})/\mu_f$
T_{in}	jet inlet temperature
T_{tci}	temperature measured by thermocouple tc$i$ ($i = 1$–4)
ΔT_{sat}	superheat, $T_s - T_{sat}$
ΔT_{sub}	subcooling, $T_{sat} - T_{in}$
u	velocity component in x direction
U_i	Cartesian component of velocity
U_{jet}	mean jet velocity
v	velocity component in y direction
w	velocity component in z direction
W	width of unit cell
W_{ch}	width of channel
W_{jet}	jet width
W_w	half-width of wall separating channels
x, y, z	Cartesian coordinates

Greek symbols

ε	dissipation rate of turbulent kinetic energy
μ	dynamic viscosity
μ_t	eddy viscosity
ν	kinematic viscosity
ρ	density
σ_ε, σ_k	empirical constants in k and ε transport equations

Subscripts

corr	correlated
exp	experimental
f	fluid
in	inlet
m	maximum (CHF)
s	test surface; solid
sat	saturation
sub	subcooling
tc$i$	thermocouple ($i = 1$–4)
th	thermocouple reading
w	channel sidewall
Γ	interface between solid and liquid

requirements, and reduced overall weight and volume of cooling hardware [9–13].

Single-phase jet-impingement cooling has also been investigated both experimentally [14–17] and numerically [18–20]. Downs and James [16] discussed the use of multiple jets to enhance cooling performance. Wadsworth and Mudawar [17] conducted confined slot-jet experiments using FC-72 as working fluid and developed a new correlation for single-phase heat transfer coefficient. Baydar and Ozmen [19] numerically simulated confined high Reynolds number impinging air jets. They showed the k–ε turbulence model is capable of accurately predicting flow characteristics. Experimental studies of two-phase jet impingement show vast superiority in cooling performance compared to single-phase jet impingement [21–25].

Recently, the authors of the present study proposed combining the attributes of micro-channel flow and jet impingement in what they termed *hybrid cooling schemes*. By introducing coolant gradually into micro-channels in the form of slot jets [26,27] or circular jets [28,29], these modules capitalize upon the high heat removal capabilities of both cooling configurations while reducing both the axial surface temperature gradient and high pressure drop of conventional micro-channel heat sinks.

In this study, a new type of micro-channel/slot-jet hybrid cooling module is examined in which liquid HFE-7100 is fed from a slot jet into each micro-channel in a modified micro-channel heat sink. This hybrid module also capitalizes upon indirect refrigeration cooling of the primary coolant (HFE-7100) to both enhance heat removal

and reduce surface temperature. Numerical simulation is used to assess the effectiveness of conventional computational tools at predicting single-phase heat transfer characteristics of the module, as well as to select a practical cooling geometry that could provide superior heat transfer coefficients and better surface temperature uniformity. Also presented is a single-phase heat transfer coefficient correlation based on a superpositioning technique that seeks to assign dominant heat transfer mechanisms to different portions of the heat transfer area. Finally, the two-phase cooling characteristics of the module are examined and a correlation for the nucleate boiling heat transfer coefficient developed.

2. Experimental methods

2.1. Flow loop

Fig. 1 shows the flow control system that was configured to supply dielectric liquid HFE-7100 to a test module housing the hybrid cooling configuration at a controlled flow rate, pressure and temperature. A primary loop containing the test module consists of a reservoir, a centrifugal pump, and a Coriolis flow meter. Throttling valves are situated both upstream and downstream of the test module to simultaneously control both flow rate and outlet pressure. The temperature of HFE-7100 is greatly reduced by sensible heat exchange to refrigerant in a two-stage cascade chiller.

2.2. Test module

Fig. 2 illustrates the layered construction and assembly of the test module. It is comprised of a heating block, a micro-jet plate, an upper plenum plate, a lower support plate, and 16 cartridge heaters. The heating block, which is machined from a single block of oxygen-free copper, is tapered in two steps to help ensure uniform temperature along the top surface. The micro-channels are cut into the 2 cm long by 1 cm wide top surface of the heating block. Five 1 mm wide and 3 mm deep micro-slots are machined within the 1 cm width of the top surface. Power is supplied to the micro-channels from the 16 cartridge heaters that are inserted into the large underside of the heating block. The slot-jet plate, which is also fabricated from oxygen-free copper, has five parallel 0.6 mm wide by 1.65 mm deep and 2.94 mm long slots machined equidistantly, facing the micro-channels of the heating block. The top plenum plate and lower support plate are both fabricated from thermally insulating G-11 fiberglass plastic.

Six type-T thermocouples are inserted below the top surface of the heating block to measure stream-wise temperature distribution. Two sets of absolute pressure transducers and type-T thermocouples are connected to the inlet and the outlet plenums. The cartridge heaters are connected in a combined series/parallel circuit and powered by a single 0–110 VAC variac. The total electrical power input is measured by a Yokogawa WT 210 wattmeter. To minimize heat loss to the ambient, the heating block is wrapped in

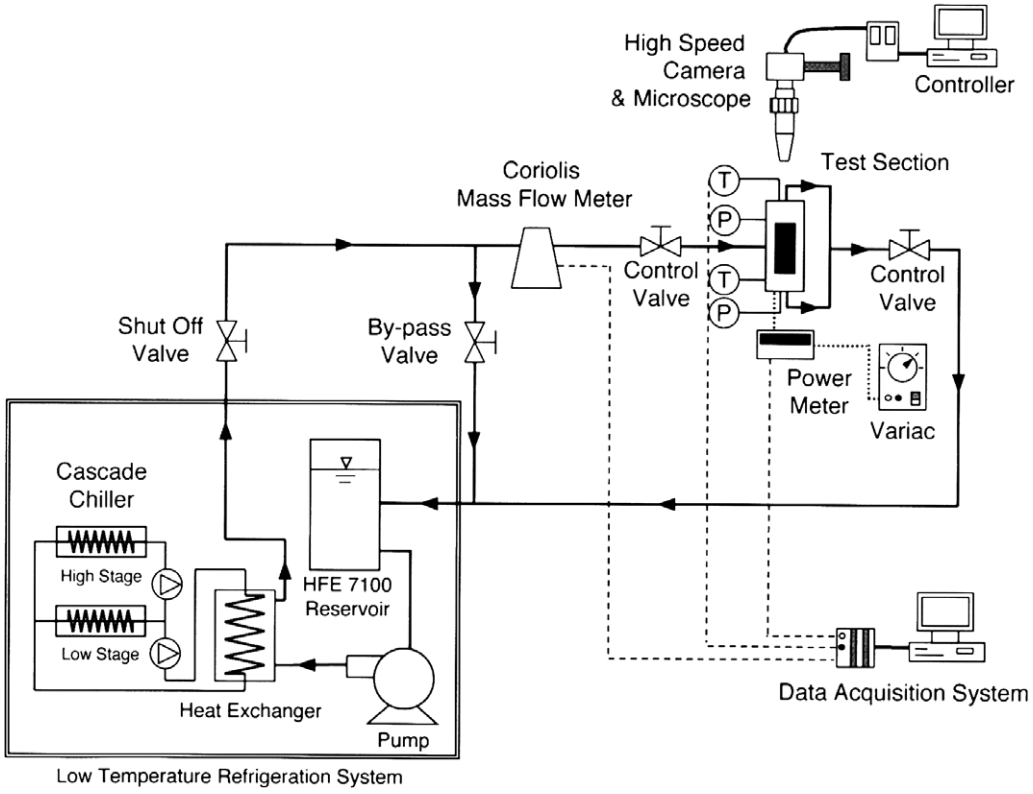

Fig. 1. Schematic of flow control system.

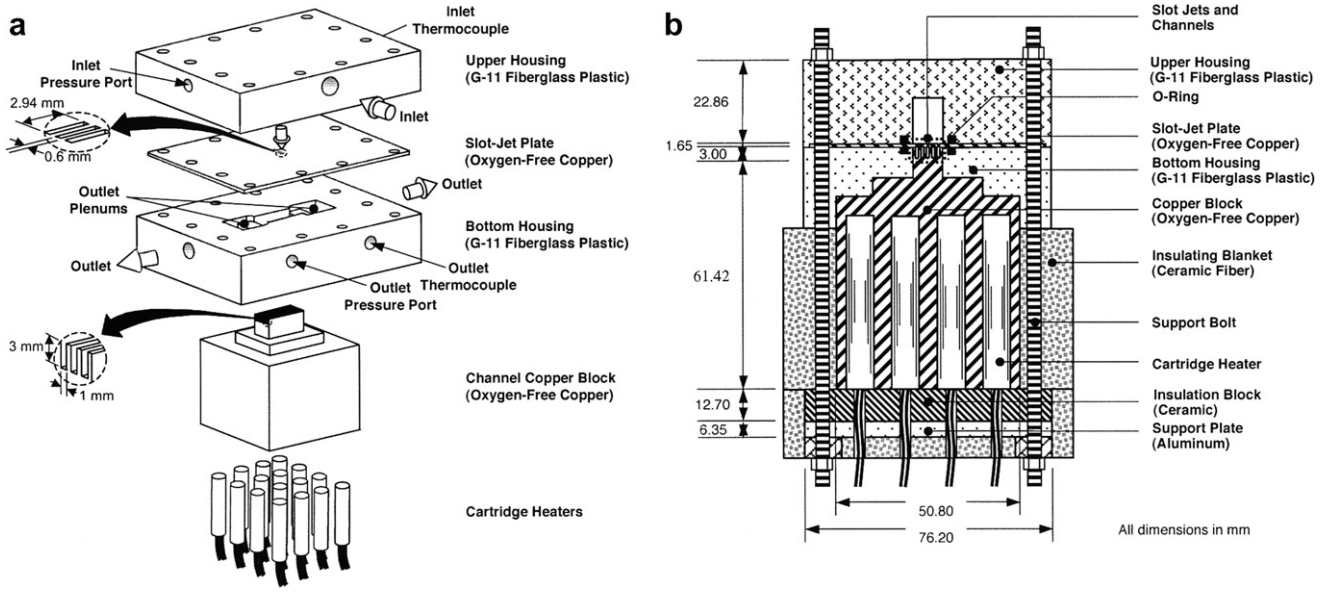

Fig. 2. (a) Test module construction. (b) Cross-section of module assembly.

Table 1
Experimental operating conditions

Working fluid	Inlet temperature T_{in} (°C)	Inlet velocity U_{jet} (m/s)	Effective heat flux, q''_{eff} (W/cm^2)
HFE-7100	−40 to 20	0.39–7.37	10.1–305.9

multiple layers of ceramic fiber and mounted atop a solid ceramic insulating plate.

Measurement uncertainties associated with the pressure transducers, flow meter, wattmeter, and thermocouples are 0.5%, 0.1%, 0.5%, and 0.3 °C, respectively. A numerical 3D thermal model of the entire test module predicts heat loss of less than 8% of the electrical power input. The heat fluxes presented in this study are therefore based on the measured electrical power input.

Table 1 summarizes the experimental operating conditions of the present study.

3. Numerical scheme

Fig. 3 shows a unit cell of the hybrid configuration that is used in the single-phase computational simulation. The unit cell consists of one of the five micro-channels along with the associated single slot jet and surrounding solid. Key dimensions of the unit cell are given in Table 2. Because of symmetry, the computational domain consists of only one quarter of the unit cell.

The finite volume method solver FLUENT 6.2.16 [30] is used to predict flow profiles and heat transfer characteristics of the hybrid scheme. The geometry and meshes are generated using Gambit 2.2.30 [31]. The standard k–ε turbulent model [32] is used for closure of the Reynolds stress tensor.

The governing equations are expressed in the Cartesian tensor notation for steady, turbulent and incompressible flow with constant properties as follows.

For the fluid region:

$$\frac{\partial U_i}{\partial x_i} = 0, \tag{1}$$

$$\rho_f U_j \frac{\partial U_i}{\partial x_j} = -\frac{\partial P}{\partial x_i} + \frac{\partial}{\partial x_j}\left((\mu_f + \mu_t)\frac{\partial U_i}{\partial x_j}\right), \tag{2}$$

and

$$\rho_f c_{p,f} U_j \frac{\partial T}{\partial x_j} = \frac{\partial}{\partial x_j}\left(\left(k_f + \frac{c_{p,f}\mu_t}{Pr_t}\right)\frac{\partial T}{\partial x_j}\right), \tag{3}$$

where

$$\mu_t = \frac{C_\mu \rho_f k^2}{\varepsilon}, \tag{4}$$

$$\rho_f U_j \frac{\partial k}{\partial x_j} = \frac{\partial}{\partial x_j}\left(\left(k_f + \frac{\mu_t}{\sigma_k}\right)\frac{\partial k}{\partial x_j}\right) + G - \rho_f \varepsilon, \tag{5}$$

and

$$\rho_f U_j \frac{\partial \varepsilon}{\partial x_j} = \frac{\partial}{\partial x_j}\left(\left(k_f + \frac{\mu_t}{\sigma_\varepsilon}\right)\frac{\partial \varepsilon}{\partial x_j}\right) + C_1 G\frac{\varepsilon}{k} - C_2\rho_f\frac{\varepsilon^2}{k}. \tag{6}$$

The production of turbulent energy is defined as $G = -\overline{u_i u_j}\partial U_i/\partial x_j$. The following values are used for the turbulent constants in the above equations: $C_\mu = 0.09$, $C_1 = 1.44$, $C_2 = 1.92$, $\sigma_k = 1.0$, $\sigma_\varepsilon = 1.3$, and $Pr_t = 0.85$.

For the solid region:

$$U_i = 0, \tag{7}$$

and

$$\frac{\partial}{\partial x_j}\left(k_s \frac{\partial T}{\partial x_j}\right) = 0. \tag{8}$$

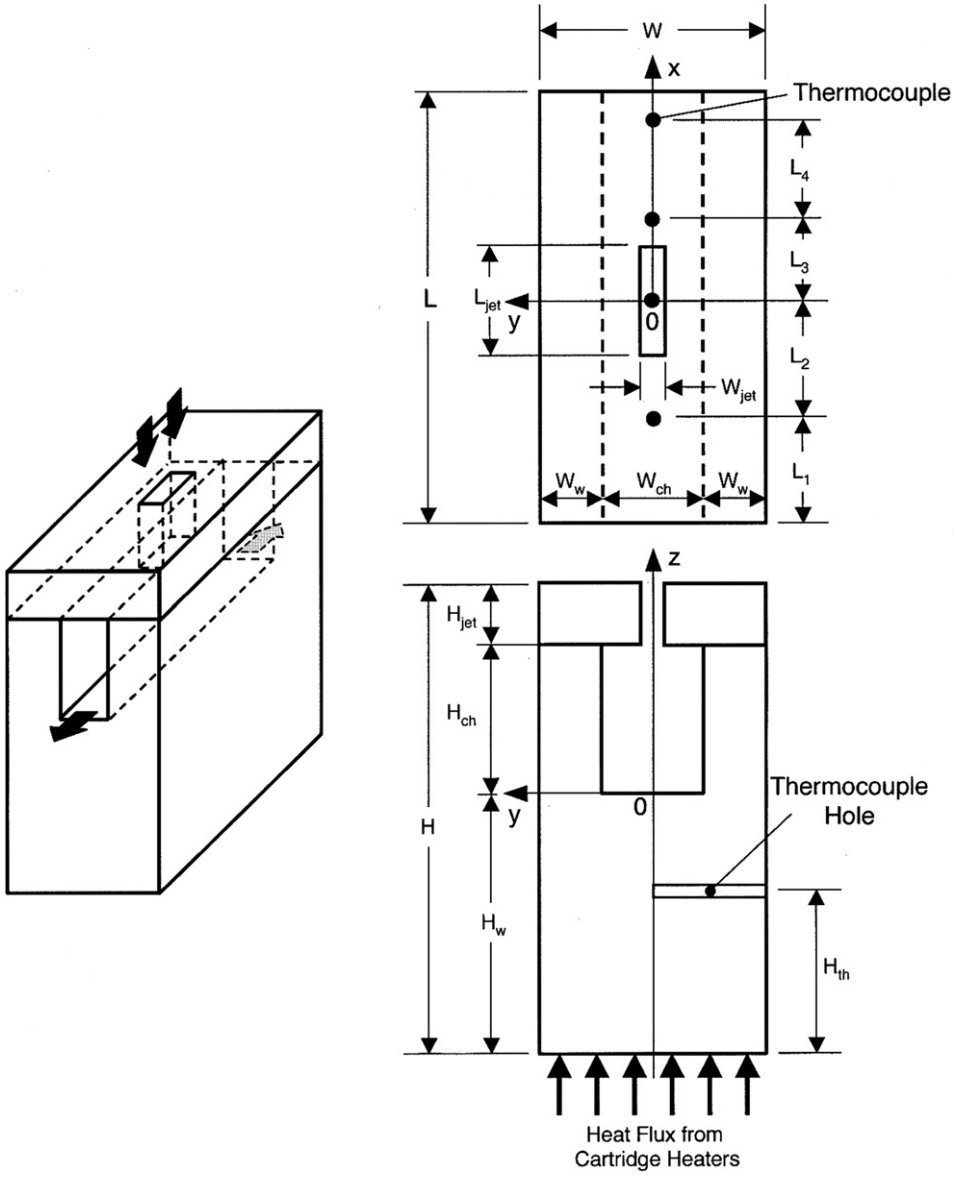

Fig. 3. Schematic of unit cell consisting of single slot jet and single micro-channel.

Table 2
Key dimensions of unit cell

L (mm)	L_1 (mm)	L_2 (mm)	L_3 (mm)	L_4 (mm)	L_{jet} (mm)	W (mm)	W_{jet} (mm)
20.00	4.00	6.00	3.00	6.00	2.94	1.83	0.60
W_{ch} (mm)	W_w (mm)	H (mm)	H_{jet} (mm)	H_{ch} (mm)	H_w (mm)	H_{th} (mm)	
1.00	0.42	14.27	1.65	3.00	7.62	5.08	

Boundary conditions are specified as follows:

$$u = 0,\ v = 0,\ w = -U_{jet} \text{ and } T = T_{in} \text{ for the jet inlet,} \quad (9)$$

$$\text{and } \dot{m} = \dot{m}_{in},\ \frac{\partial v}{\partial x} = 0,\ \frac{\partial w}{\partial x} = 0 \text{ and } \frac{\partial T}{\partial x} = 0$$

for the channel outlet. (10)

A constant heat flux is applied along the bottom surface of the unit cell,

$$-k_s \frac{\partial T}{\partial z} = q''_{eff}, \quad (11)$$

where q''_{eff} is determined from the measured electrical power input as

$$q''_{eff} = \frac{P_W}{A_t}. \quad (12)$$

Adiabatic conditions are applied to all solid thermal boundaries except the interfaces between HFE-7100 and copper. The Semi-Implicit Method for Pressure-Linked Equations (SIMPLE) algorithm [33] is used to couple velocities and pressure. To examine the effects of mesh size, 84,000, 288,000 and 517,500 mesh elements were tested. The middle mesh size was used because temperature differences were less than 3.2% of the finer mesh.

4. Numerical results

4.1. Effects of micro-channel geometry

A numerical parametric study was conducted by varying micro-channel height, H_{ch}, micro-channel wall thickness, W_w, and jet width, W_{jet}, as indicated in Table 3. Fig. 4a shows the effects of micro-channel height on surface centerline temperature for $W_w = 0.43$ mm, $W_{jet} = 0.6$ mm and jet velocities of $U_{jet} = 5$ and 10 m/s. The higher jet velocity is shown decreasing the maximum surface temperature appreciably. Due to the fin effect of the micro-channel copper sidewall, a lower axial temperature gradient is achieved at $U_{jet} = 5$ m/s for $H_{ch} = 3$ mm compared to 1 mm. This effect appears to subside appreciably for $U_{jet} = 10$ m/s because of apparent dominance of jet impingement with the channel's bottom wall compared to the fin effect.

Fig. 4b shows that surface temperature is reduced for $U_{jet} = 5$ m/s by decreasing channel width because stronger jet vorticity along the channel sidewalls increases the contribution of sidewall conduction. Additionally, mean flow velocity along the micro-channel increases with decreasing W_{ch}, which helps decrease the axial temperature gradient as well. For a fixed W_{ch}, decreasing jet width, W_{jet}, in half while maintaining the same flow rate requires doubling jet velocity. Fig. 4b shows higher jet velocity decreases surface temperature, although the axial temperature gradient is greater. This trend points to a very important practical conclusion concerning maximum surface temperature: for a given flow rate, higher heat transfer coefficients and lower surface temperatures are possible simply by decreasing jet width. Obvious limits to how small jet width can be made are manufacturability and high pressure drop.

4.2. Validation of numerical predictions

Fig. 5 compares numerical predictions with temperatures measured along the thermocouple line beneath the test surface. Both the data and predicted results show temperature decreases with increasing Reynolds number, decreasing heat flux and decreasing coolant inlet tempera-

Table 3
Dimensions tested in numerical parametric study

H_{ch} (mm)	W_{ch} (mm)	W_{jet} (mm)	U_{jet} (m/s)
1.00, 3.00	1.00, 1.40	0.30, 0.60	5, 10

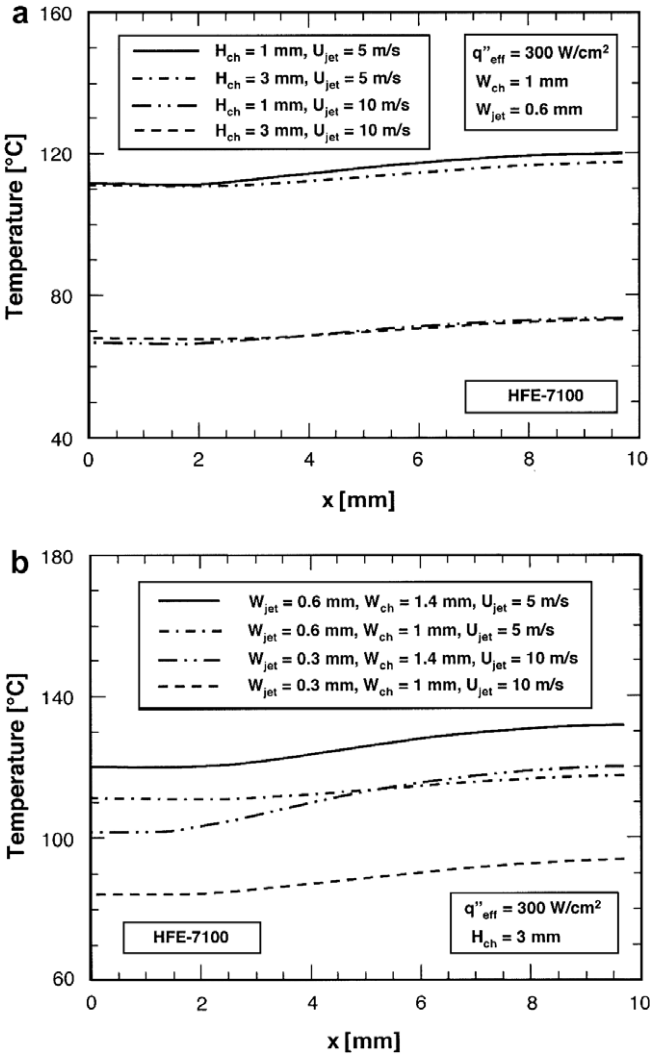

Fig. 4. Numerical predictions of the effects of (a) channel height and (b) jet width and channel width on centerline temperature distribution along micro-channel.

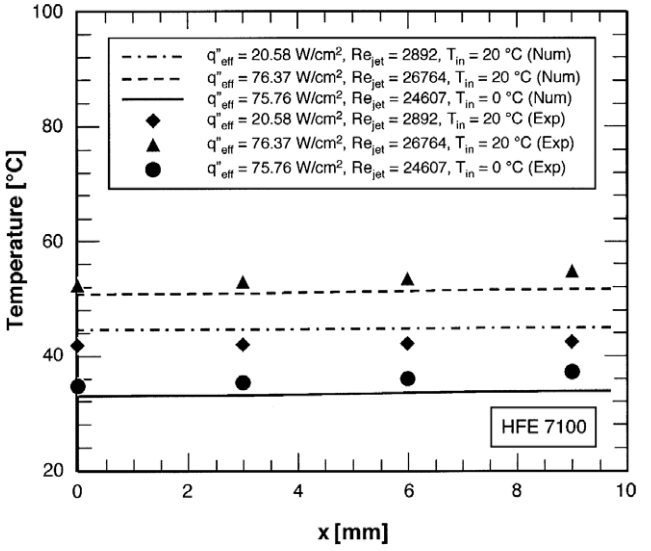

Fig. 5. Comparison of numerical predictions of temperatures along thermocouple line with measured temperatures.

ture. Excellent agreement between numerical predictions and experimental results shows the conventional Navier–Stokes and energy equations with the k–ε turbulence model can accurately predict the heat transfer characteristics of the present hybrid configuration.

4.3. Predicted trends of single-phase cooling performance

Fig. 6a and b shows temperature distribution of the micro-channel bottom wall of the unit cell, including the sidewall, for $q''_{\text{eff}} = 20.58\ \text{W/cm}^2$ with $Re_{\text{jet}} = 2892$ and $q''_{\text{eff}} = 76.37\ \text{W/cm}^2$ with $Re_{\text{jet}} = 26{,}764$, respectively. Overall, surface temperature increases along the micro-channel flow direction, and higher temperatures are encountered near the outlet. Comparing the two figures shows higher jet velocities decrease surface temperature. Slightly lower surface temperatures are achieved below the sidewall due to the aforementioned fin effect. Along the centerline of the micro-channel bottom wall, Fig. 6a shows the lowest surface temperature is achieved immediately below the center of the slot jet ($x = 0$). However, the lowest temperature of the channel bottom wall is located near the end of the

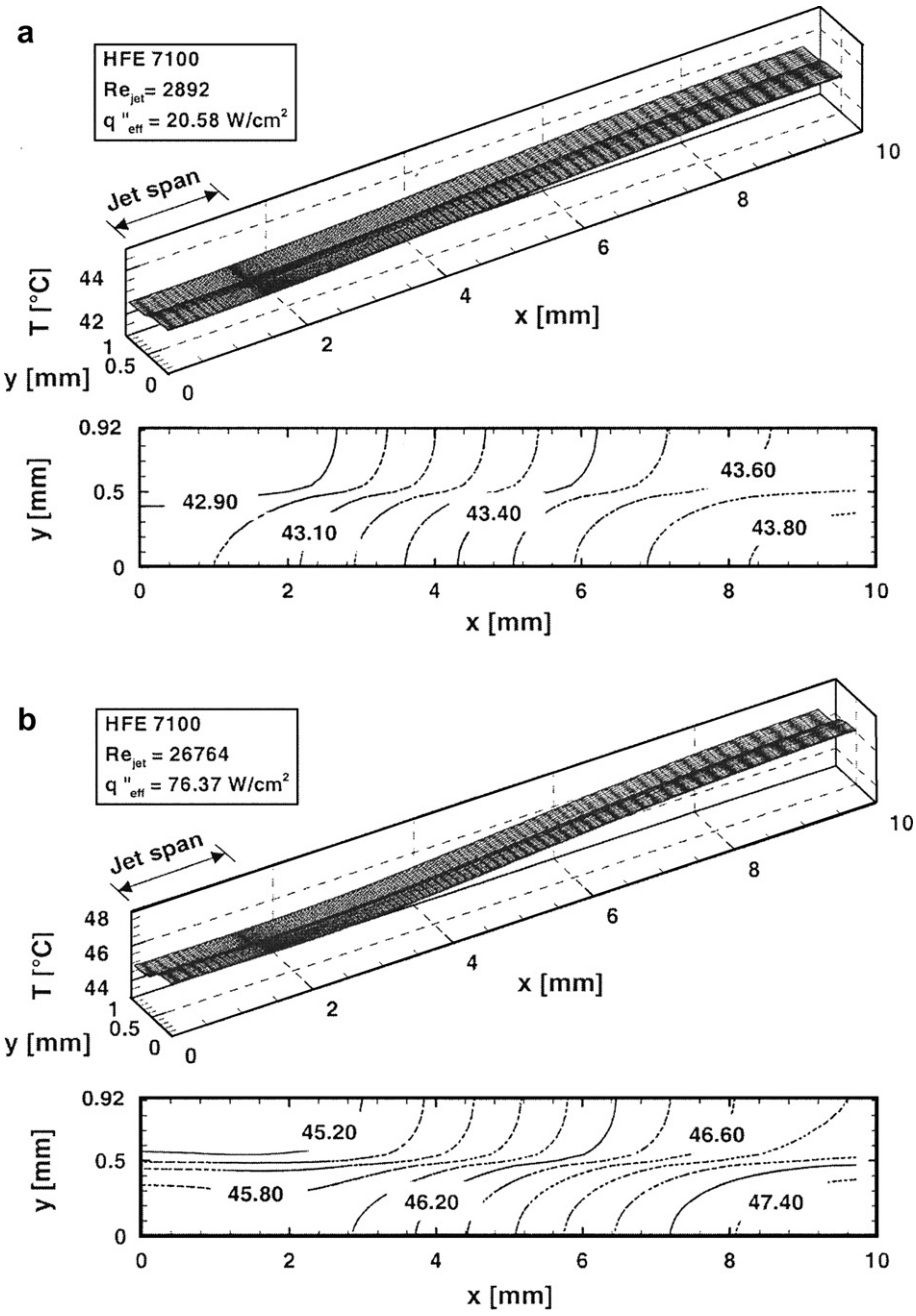

Fig. 6. Numerical predictions of micro-channel bottom wall temperature distribution including sidewall for (a) $Re_{\text{jet}} = 2892$ and $q''_{\text{eff}} = 20.58\ \text{W/cm}^2$, and (b) $Re_{\text{jet}} = 26{,}764$ and $q''_{\text{eff}} = 76.37\ \text{W/cm}^2$.

slot jet span because of increased velocity along the micro-channel.

Figs. 7 and 8 show the heat flux distribution along the micro-channel bottom wall and the sidewall, respectively. The local heat flux is evaluated from

$$q'' = -k_\Gamma \frac{\partial T_\Gamma}{\partial n}\bigg|_\Gamma, \tag{13}$$

where k_Γ is the interface thermal conductivity obtained by the harmonic mean of k_s and k_f.

Both distributions in Fig. 7 show heat flux is greatest near the jet centerline due to the impingement effect and thin boundary layer. Notice how the heat flux becomes vanishingly small in the lower corner of the micro-channel where the flow is highly weakened for the rectangular channel.

Fig. 8a and b shows a sharp rise in heat flux along the sidewall a short distance above the test surface. This rise is the result of the wall jet forming away from the stagnation zone of the slot jet. Notice the stronger influence of this wall jet in Fig. 8b for the higher Reynolds number case. The wall jet flow also induces strong circumferential recirculation, producing high fluxes along the entire sidewall, which is obviously being sustained by heat conduction along the sidewall.

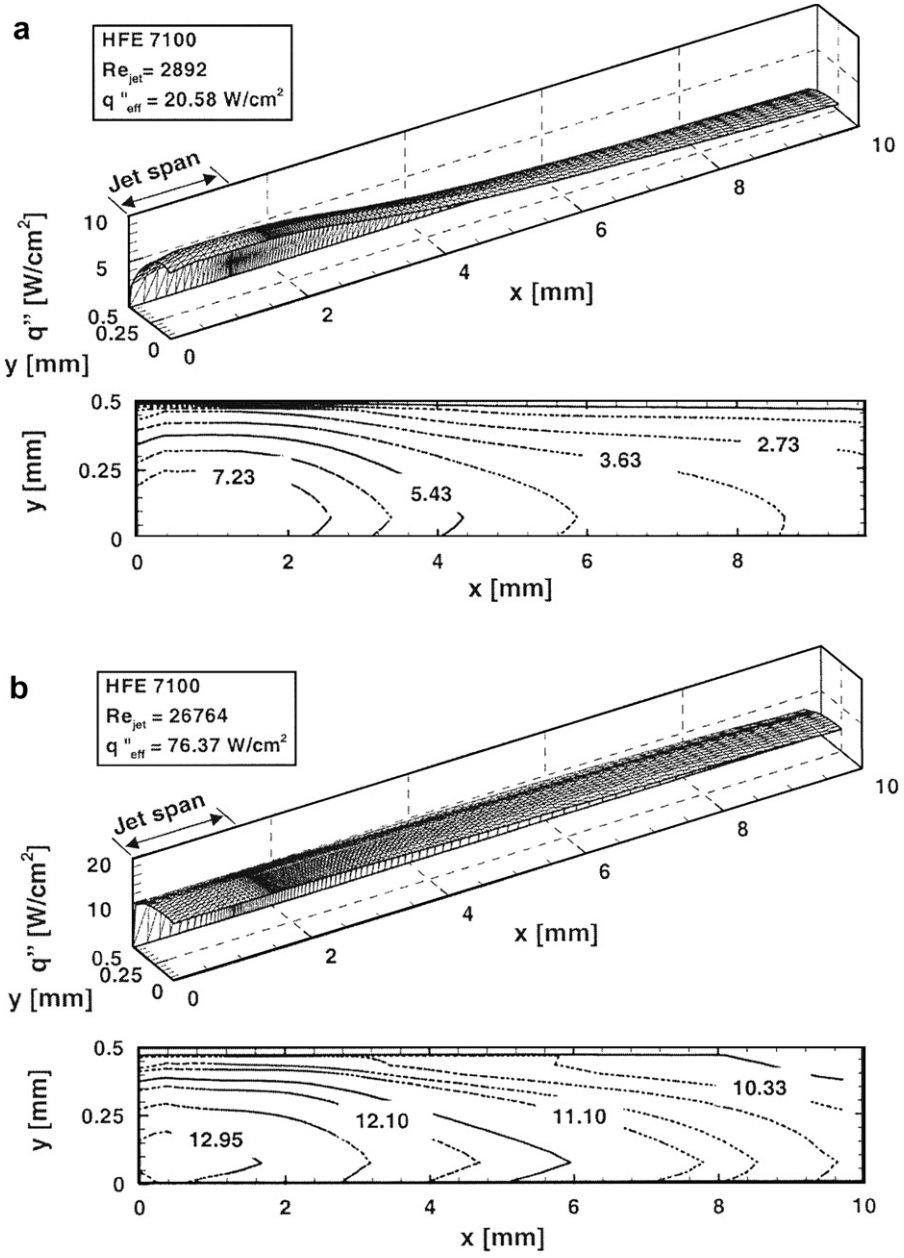

Fig. 7. Numerical predictions of micro-channel bottom wall heat flux distribution for (a) $Re_{jet} = 2892$ and $q''_{eff} = 20.58$ W/cm^2, and (b) $Re_{jet} = 26{,}764$ and $q''_{eff} = 76.37$ W/cm^2.

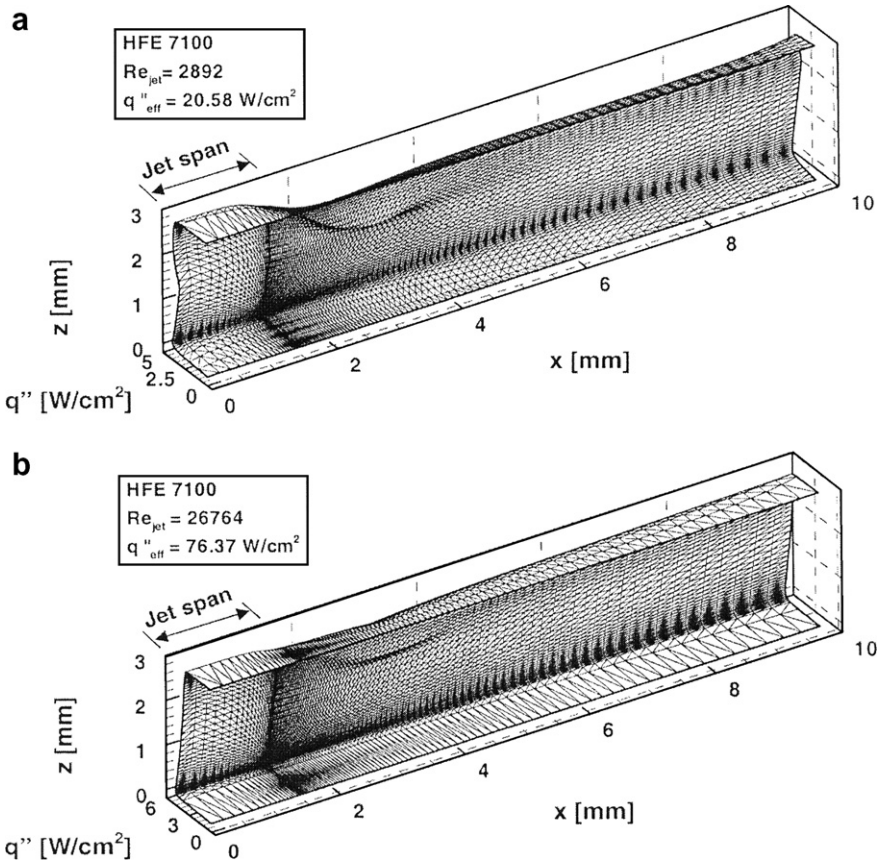

Fig. 8. Numerical predictions of micro-channel sidewall heat flux distribution for (a) $Re_{jet} = 2892$ and $q''_{eff} = 20.58$ W/cm^2, and (b) $Re_{jet} = 26{,}764$ and $q''_{eff} = 76.37$ W/cm^2.

Fig. 9 shows local Nusselt number along the micro-channel's bottom wall follows a distribution similar to that shown in Fig. 7 for heat flux. The local Nusselt number is defined as

$$Nu = \frac{q'' d_h}{k_f (T_s - T_{in})}. \tag{14}$$

5. Single-phase experimental results

5.1. Overall cooling performance

Choice of key geometrical parameters of the test module is based largely on the numerical findings. Key goals in the module design are to enhance heat flux removal, reduce surface temperature, and reduce surface temperature gradients. Fig. 10 shows thermocouple readings in the copper heating block as a function of Reynolds numbers for $q''_{eff} = 32$ W/cm^2. Increasing Reynolds number decreases both surface temperature and temperature gradient. Despite the relatively poor thermophysical properties of HFE-7100, the high cooling effectiveness of the hybrid configuration, coupled with the use of indirect refrigeration cooling, enables the dissipation of $q''_{eff} = 305.9$ W/cm^2 at $T_{in} = -40$ °C and $U_{jet} = 7.37$ m/s *without* phase change. At this heat flux, the average surface temperature is 70.82 °C, well below the maximum recommended temperature for modern electronic devices. Surface temperature variations up to $q''_{eff} = 50$ W/cm^2 are less than 2 °C.

5.2. Single-phase correlation

A new single-phase heat transfer correlation is sought for the hybrid configuration. A superposition technique is employed that consists of dividing the heat transfer area into different regions that are each dominated by a different heat transfer mechanism. This technique was recommended by Wadsworth and Mudawar [17] for slot jet cooling and has been quite effective at correlating the present authors' own single-phase data for a hybrid micro-channel/micro-jet-impingement module [29].

Fig. 11 illustrates the different surface heat transfer regions used in the present superpositioning technique. The general single-phase correlation form:

$$\frac{\overline{Nu}_L}{Pr_f^{0.4}} = f(Re) \tag{15}$$

is applied to each of these regions. The surface is comprised of an impingement region, two identical sidewall regions, and two identical channel flow regions. Using the superpositioning technique, the overall heat transfer is represented by the relation:

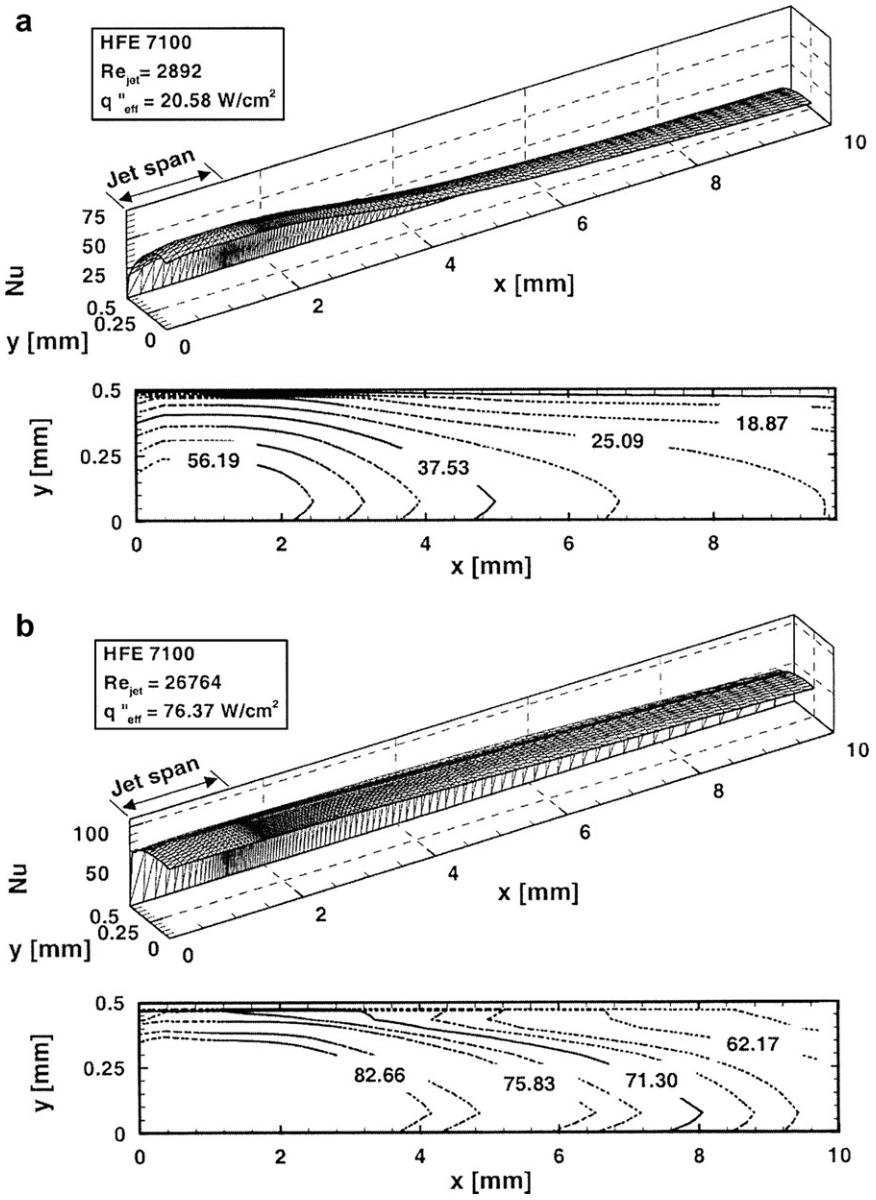

Fig. 9. Numerical predictions of micro-channel bottom wall Nusselt number distribution for (a) $Re_{jet} = 2892$ and $q''_{eff} = 20.58\ W/cm^2$, and (b) $Re_{jet} = 26{,}764$ and $q''_{eff} = 76.37\ W/cm^2$.

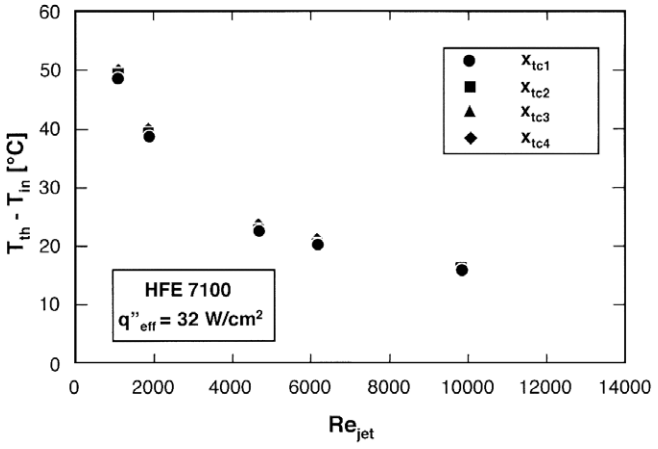

Fig. 10. Thermocouple readings inside heater block versus jet Reynolds number for $q''_{eff} = 32\ W/cm^2$.

$$\overline{Nu}_L = \frac{\bar{h}_L L}{k_f} = \left(\frac{\overline{h}_{jet}\left(\frac{W_{jet}L_{jet}}{p_h}\right)}{k_f}\right) + \left(\frac{\overline{h}_{ch1}\left(L_{jet} - \frac{2W_{jet}L_{jet}}{p_h}\right)}{k_f}\right) + \left(\frac{\overline{h}_{ch2}(L - L_{jet})}{k_f}\right). \quad (16)$$

The Reynolds numbers for these regions are given by

$$Re_{jet} = \frac{U_{jet}(2W_{jet})}{\nu_f},$$

$$Re_{ch1} = \frac{U_{ch1}\left(L_{jet} - \frac{2W_{jet}L_{jet}}{p_h}\right)}{\nu_f}, \quad \text{and}$$

$$Re_{ch2} = \frac{U_{ch2}(L - L_{jet})}{\nu_f}. \quad (17)$$

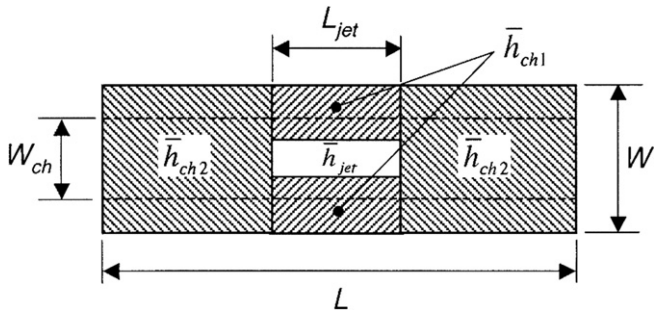

Fig. 11. Schematic of superpositioning technique for correlating single-phase heat transfer data.

For an impinging jet, sidewall characteristic velocity is fairly equal to jet exit velocity due the Bernoulli effect. On the other hand, the channel velocity can be determined from mass conservation.

$$U_{ch1} = U_{jet}, U_{ch2} = U_{jet}\frac{L_{jet}W_{jet}}{H_{ch}W_{ch}}. \tag{18}$$

Therefore, the hybrid module's heat transfer correlation can be written as

$$\begin{aligned}\frac{\overline{Nu}_L}{Pr_f^{0.4}} &= C_1 Re_{jet}^a\left(\frac{L_{jet}}{p_h}\right) + C_2 Re_{ch1}^b + C_3 Re_{ch2}^c \\ &= C_1 Re_{jet}^a\left(\frac{L_{jet}}{p_h}\right) + C_2 Re_{jet}^b\left(\frac{L_{jet}}{2W_{jet}} - \frac{L_{jet}}{p_h}\right)^b \\ &\quad + C_3 Re_{jet}^c\left(\frac{L_{jet}(L-L_{jet})}{H_{ch}W_{ch}}\right)^c.\end{aligned} \tag{19}$$

Wadsworth and Mudawar [11] showed the impingement term can be accurately characterized by setting $a = 0.5$, which is also adopted in the present correlation. The remaining empirical constants are determined by a least-squares' fit to the present experimental data. Two separate correlations were obtained depending on jet Reynolds number. The first is a high Re_{jet} correlation that is valid for $3232 < Re_{jet} < 30{,}853$,

$$\begin{aligned}\frac{\overline{Nu}_L}{Pr_f^{0.4}} &= 1.53 Re_{jet}^{0.5}\left(\frac{L_{jet}}{p_h}\right) + 5.01 Re_{jet}^{0.6}\left(\frac{L_{jet}}{2W_{jet}} - \frac{L_{jet}}{p_h}\right)^{0.6} \\ &\quad + 0.18 Re_{jet}^{0.46}\left(\frac{L_{jet}(L-L_{jet})}{H_{ch}W_{ch}}\right)^{0.46}.\end{aligned} \tag{20}$$

The second, low Re_{jet} correlation, is valid for $751 < Re_{jet} < 3232$,

$$\begin{aligned}\overline{Nu}_L &= 1.53 Re_{jet}^{0.5}\left(\frac{L_{jet}}{p_h}\right) Pr_f^{0.4} + 1.3 Re_{jet}^{0.45}\left(\frac{L_{jet}}{2W_{jet}} - \frac{L_{jet}}{p_h}\right)^{0.45} \\ &\quad + 9.99 Re_{jet}^{0.52}\left(\frac{L_{jet}(L-L_{jet})}{H_{ch}W_{ch}}\right)^{0.52}.\end{aligned} \tag{21}$$

Fig. 12 shows Eqs. (20) and (21) fit the entire HFE-7100 database with a mean absolute error (MAE) of 3.90%.

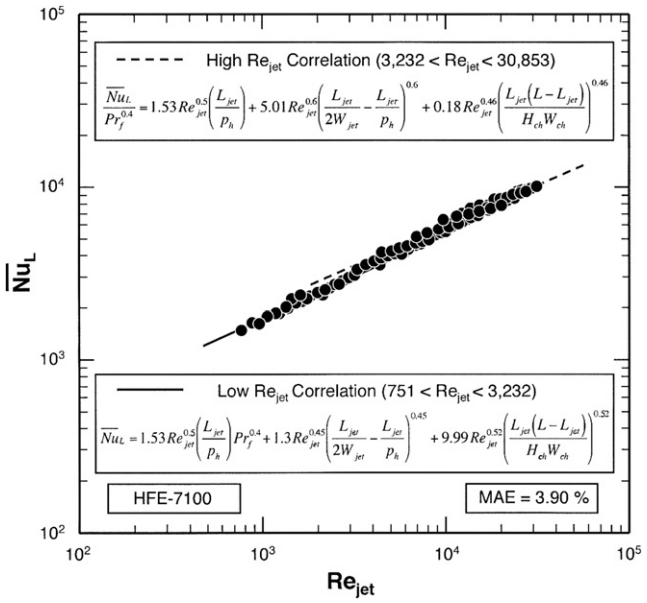

Fig. 12. Comparison of predictions of single-phase heat transfer coefficient correlations with HFE-7100 data.

6. Two-phase experimental results

6.1. Boiling curve trends

Fig. 13a and b shows boiling curves obtained from the four thermocouple readings for a jet velocity of $U_{jet} = 0.87$ m/s and inlet subcoolings of $\Delta T_{sub} = 88.1$ and 68.1 °C, respectively. For each subcooling, the slope of the boiling curve in the single-phase region is fairly constant, indicative of a constant heat transfer coefficient. The highest temperature in the same region is encountered near the outlet, which is consistent with the previous single-phase numerical predictions. For both subcoolings, location x_{tc4} shows the earliest increase in slope, making the onset of boiling near the outlet. This location also maintains the highest temperatures throughout the nucleate boiling region and is where critical heat flux (CHF) commences. CHF values for the conditions of Fig. 13a and b are 310.6 and 243.3 W/cm^2, respectively.

Fig. 14a shows the effects of subcooling on the boiling curve for $U_{jet} = 0.86$ m/s. Slight deviations in the single-phase region are the result of liquid property variations with temperature. Increasing the subcooling delays the onset of boiling incipience and enhances CHF considerably. Increased CHF is the result of the subcooled liquid's ability to absorb a substantial fraction of the wall heat flux in the form of sensible heat prior to evaporation. Fig. 14b shows the effects of jet velocity (and flow rate) on the boiling curve for $\Delta T_{sub} = 107.8$ °C. Increasing U_{jet} delays the onset of boiling and broadens the single-phase heat transfer region considerably. CHF also increases appreciably with increasing U_{jet}. Because of high CHF values, higher velocity tests were terminated well before CHF to protect the test module against potential overheating or burnout.

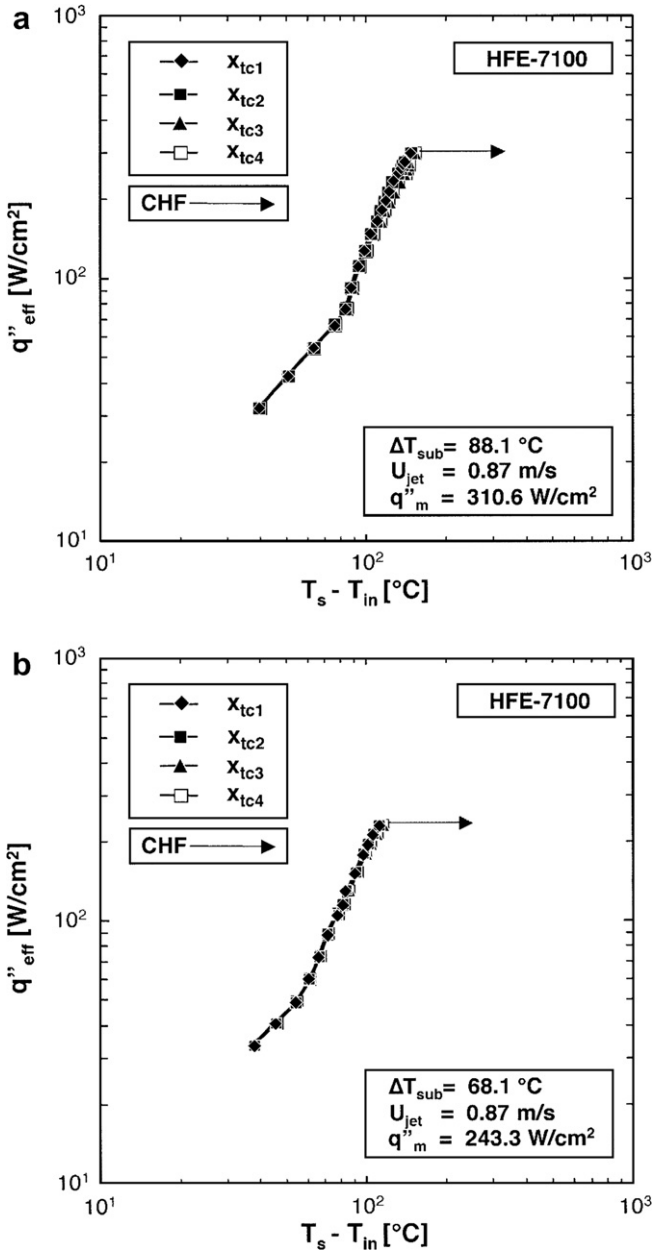

Fig. 13. Boiling curves measured at x_{tc1}, x_{tc2}, x_{tc3} and x_{tc4} for $U_{jet} = 0.87$ m/s at (a) $\Delta T_{sub} = 88.1$ °C and (b) $\Delta T_{sub} = 68.1$ °C.

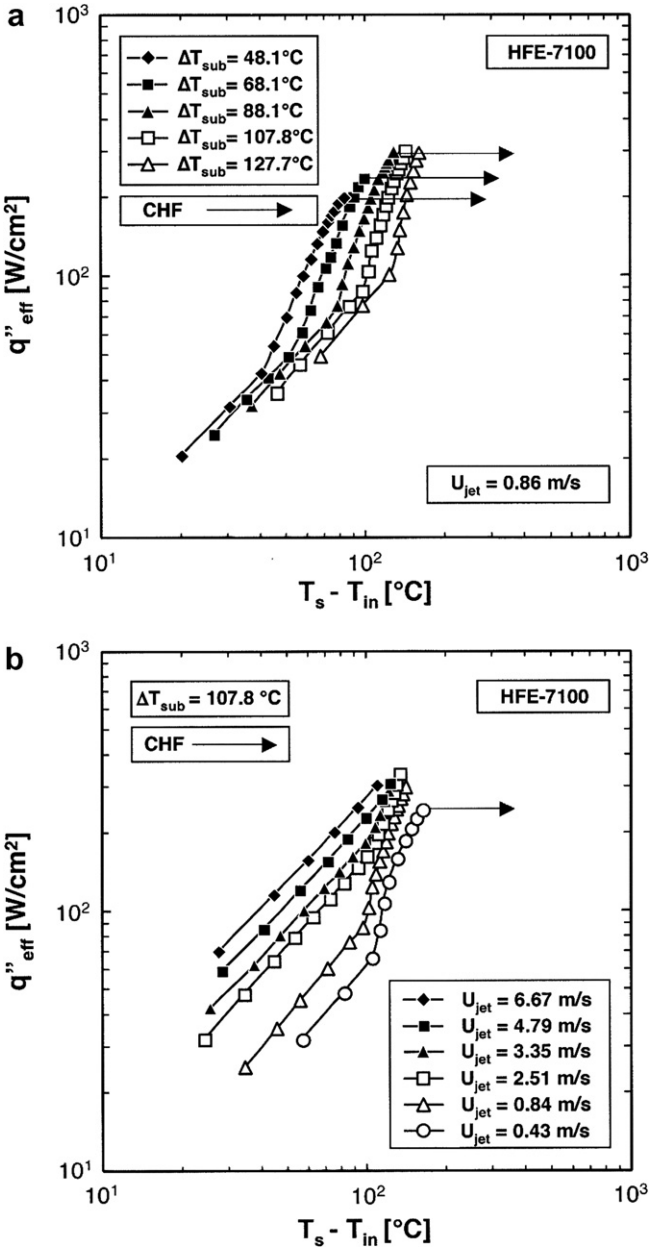

Fig. 14. (a) Subcooling effects on boiling curve at $U_{jet} = 0.86$ m/s. (b) Jet velocity effects on boiling curve at $\Delta T_{sub} = 107.8$ °C.

6.2. Flow visualization results

To capture two-phase flow behavior along the micro-channels, the test module's jet plate and upper housing (see Fig. 2) were replaced with plates made from transparent polycarbonate plastic (Lexan). A high-speed video camera fitted with close-up lenses was positioned above the test module as illustrated in Fig. 1. This placement facilitated viewing of three adjacent micro-channels. The relatively low melting point of polycarbonate plastic limited these flow visualization tests to low heat fluxes. Fig. 15a and b shows representative images captured at $U_{jet} = 0.44$ m/s and $\Delta T_{sub} = 48.1$ °C at $q''_{eff} = 43$ and 63 W/cm^2, respectively. Fig. 15a shows a combination bubbly flow, caused by sidewall nucleation, and slug flow. Increasing the heat flux causes further bubble coalescence into longer slug bubbles as depicted in Fig. 15b. Notice the appreciable increase in void fraction, evidenced by the large size of bubbles exiting the micro-channels in Fig. 15b compared to Fig. 15a.

Qu and Mudawar [9] classified two types of flow instability in conventional two-phase micro-channel heat sinks, severe pressure drop oscillation and mild parallel channel instability. Severe pressure drop oscillation is the result of interaction between the two-phase flow in the micro-channel heat sink and the upstream compressible volume in the flow loop. This instability causes severe fluctuations between incoming liquid and downstream two-phase

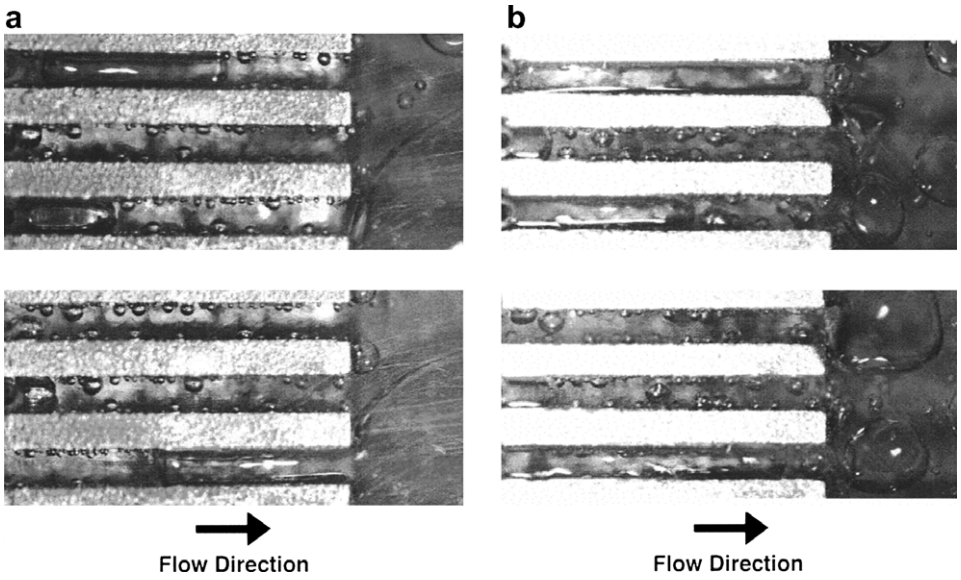

Fig. 15. Flow visualization and flow patterns inside hybrid module for $U_{jet} = 0.44$ m/s and $\Delta T_{sub} = 48.1$ °C with (a) $q''_{eff} = 43$ W/cm^2 and (b) $q''_{eff} = 63$ W/cm^2.

mixture in all channels. The mild parallel channel instability is the result of flow interactions among micro-channels and is intrinsic to the heat sink itself. Fig. 15a and b depicts the mild parallel channel instability that causes the variations in flow pattern among adjacent micro-channels. Interestingly, the severe pressure drop oscillation was never observed in the present study.

6.3. Nucleate boiling correlation

Fig. 14b shows boiling curves for different velocities have a tendency to converge in the nucleate boiling region, which is consistent with findings from previous jet-impingement studies [16,17]. However, as shown in Fig. 14a, increasing the subcooling causes a monotonic decrease in the two-phase heat transfer coefficient for a fixed heat flux.

In a previous study by the present authors [29], nucleate boiling data for a hybrid micro-channel/micro-circular-jet-impingement module were correlated using the following relations between heat flux and wall superheat,

$$q''_{eff} = C\Delta T^n_{sat}, \tag{22}$$

and

$$q''_{eff} = h(T_s - T_{in}) = h(\Delta T_{sat} + \Delta T_{sub}). \tag{23}$$

Combining these two relations yields a general relationship for the two-phase heat transfer coefficient.

$$h = \frac{q''_{eff}}{\left(\frac{q''_{eff}}{C}\right)^{1/n} + \Delta T_{sub}} \tag{24}$$

The empirical constants n and C in the above equation were obtained by a least-squares' fit to the entire nucleate boiling database for the hybrid micro-channel/micro-circular-jet configuration, resulting in the correlation:

$$h = \frac{q''_{eff}}{\left(\frac{q''_{eff}}{64.81}\right)^{1/3.252} + \Delta T_{sub}}. \tag{25}$$

Fig. 16 shows the above correlation is equally successful at predicting the present micro-channel/slot-jet data, evidenced by a mean absolute error of only 5.66%.

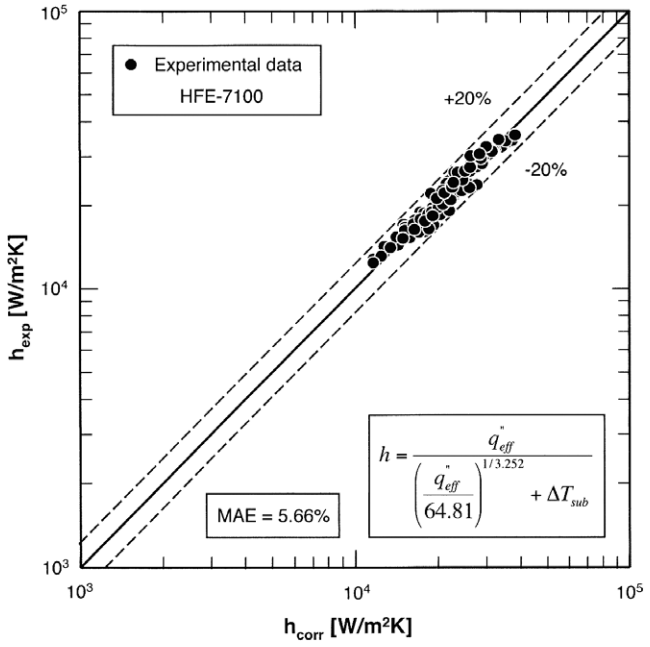

Fig. 16. Comparison of predictions of two-phase heat transfer coefficient correlation with HFE-7100 data.

7. Conclusions

This paper explored the single-phase and two-phase cooling performance of a hybrid micro-channel/slot-jet-impingement module using HFE-7100 as working fluid. The single-phase performance was examined numerically in pursuit of a geometry that yields superior heat removal capability, lower surface temperature, and smaller surface temperature gradients. This geometry was then tested experimentally to validate the numerical findings. In addition, correlations were developed for both the single-phase and two-phase heat transfer coefficients. Key findings from the study are as follows:

1. In the single-phase region, heat conduction along the micro-channel sidewalls is especially effective at relatively low impingement velocities. Increasing micro-channel height for low velocities reduces the temperature gradient along the micro-channel. Because of a stronger impingement effect, the influence of micro-channel height at high Reynolds numbers is less significant. For fixed micro-channel width and jet Reynolds number, decreasing jet width increases jet velocity, reducing surface temperature. However, decreasing jet width also increases surface temperature gradient along the micro-channel.
2. The hybrid module maintains a high degree of surface temperature uniformity. Surface temperature gradients are below 2 °C for heat fluxes up to 50 W/cm^2. Even without phase change, the hybrid module is capable of dissipating very high heat fluxes. A heat flux of 305.9 W/cm^2 is achieved with a jet velocity of 7.37 m/s and inlet temperature of −40 °C.
3. A superpositioning technique is shown to effectively capture the single-phase cooling performance. This technique enabled the development of two new correlations for the single-phase heat transfer coefficient having an overall mean absolute error of 3.43%.
4. Increasing subcooling and/or flow rate delays the onset of nucleate boiling to a higher heat flux and a higher surface temperature, as well as enhances CHF. Subcooling is especially effective at increasing CHF and therefore enabling the removal of very high heat fluxes.
5. A two-phase heat transfer correlation previously developed for a hybrid micro-channel/micro-circular-jet module is equally effective at predicting data for the present hybrid module.

Acknowledgement

The authors are grateful for the support of the Office of Naval Research (ONR) for this research.

References

[1] I. Mudawar, Assessment of high-heat-flux thermal management schemes, IEEE Trans. Compon. Pack. Technol. 24 (2001) 122–141.
[2] D.B. Tuckerman, R.F.W. Pease, High-performance heat sinking for VLSI, IEEE Electron. Dev. Lett. 2 (1981) 126–129.
[3] M.B. Bowers, I. Mudawar, High flux boiling in low flow rate, low pressure drop mini-channel and micro-channel heat sinks, Int. J. Heat Mass Transfer 37 (1994) 321–332.
[4] D. Lelea, S. Nishio, K. Takano, The experimental research on micro-tube heat transfer and fluid flow of distilled water, Int. J. Heat Mass Transfer 47 (2004) 4215–4231.
[5] A.G. Fedorov, R. Viskanta, Three-dimensional conjugate heat transfer in the microchannel heat sink for electronic packaging, Int. J. Heat Mass Transfer 43 (2000) 399–415.
[6] W. Qu, I. Mudawar, Experimental and numerical study of pressure drop and heat transfer in a single-phase micro-channel heat sink, Int. J. Heat Mass Transfer 45 (2002) 2549–2565.
[7] S.J. Kim, D. Kim, forced convection in microstructures for electronic equipment cooling, ASME J. Heat Transfer 121 (1999) 639–645.
[8] K.K. Ambatipudi, M.M. Rahman, Analysis of conjugate heat transfer in microchannel heat sinks, Numer. Heat Transfer 37 (2000) 711–731.
[9] W. Qu, I. Mudawar, Measurement and prediction of pressure drop in two-phase micro-channel heat sinks, Int. J. Heat Mass Transfer 46 (2003) 2737–2753.
[10] J. Lee, I. Mudawar, Two-phase flow in high-heat-flux micro-channel heat sink for refrigeration cooling applications: Part I – pressure drop characteristics, Int. J. Heat Mass Transfer (2005) 928–940.
[11] W. Qu, I. Mudawar, Measurement and correlation of critical heat flux in two-phase micro-channel heat sinks, Int. J. Heat Mass Transfer 47 (2004) 2045–2059.
[12] X.F. Peng, B.-X. Wang, Forced convection and flow boiling heat transfer for liquid flowing through microchannels, Int. J. Heat Mass Transfer 36 (1993) 3421–3427.
[13] M.E. Steinke, S.G. Kandlikar, An experimental investigation of flow boiling characteristics of water in parallel microchannels, ASME J. Heat Transfer 126 (2004) 518–526.
[14] H. Martin, Heat and mass transfer between impinging gas jets and solid surfaces, Adv. Heat Transfer 13 (1977) 1–60.
[15] L.M. Jiji, Z. Dagan, Experimental investigation of single-phase multi-jet impingement cooling of array of microelectronic heat sources, in: Proceedings of International Symposium on Cooling Technology for Electronic Equipment, Honolulu, HI, 1987, pp. 265–283.
[16] S.J. Downs, E.H. James, Jet impingement heat transfer – a literature survey, Paper No. 87-HT-35, ASME, New York, NY, 1987.
[17] D.C. Wadsworth, I. Mudawar, Cooling of a multichip electronic module by means of confined two-dimensional jets of dielectric liquid, ASME J. Heat Transfer 112 (1990) 891–898.
[18] T.J. Craft, L.J.W. Graham, B.E. Launder, Impinging jet studies for turbulence model assessment – II. An examination of the performance of four turbulence models, Int. J. Heat Mass Transfer 36 (1993) 2685–2697.
[19] E. Baydar, Y. Ozmen, An experimental and numerical investigation on a confined impinging air jet at high Reynolds numbers, Appl. Therm. Eng. 25 (2005) 409–421.
[20] T.H. Park, H.G. Choi, J.Y. Yoo, S.J. Kim, Streamline upwind numerical simulation of two-dimensional confined impinging slot jets, Int. J. Heat Mass Transfer 46 (2003) 251–262.
[21] Y. Katto, M. Kunihiro, Study of the mechanism of burn-out in boiling system of high burn-out heat flux, Bull. JSME 16 (1973) 1357–1366.
[22] C.F. Ma, A.E. Bergles, Jet impingement nucleate boiling, Int. J. Heat Mass Transfer 29 (1986) 1095–1101.
[23] I. Mudawar, D.C. Wadsworth, Critical heat flux from a simulated chip to a confined rectangular impinging jet of dielectric liquid, Int. J. Heat Mass Transfer 34 (1991) 1465–1479.
[24] K.A. Estes, I. Mudawar, Comparison of two-phase electronic cooling using free jets and sprays, ASME J. Electron. Pack. 117 (1995) 323–332.
[25] M.E. Johns, I. Mudawar, An ultra-high power two-phase jet-impingement avionic clamshell module, ASME J. Electron. Pack. 118 (1996) 264–270.

[26] M.K. Sung, I. Mudawar, Experimental and numerical investigation of single-phase heat transfer using a hybrid jet impingement/micro-channel cooling scheme, Int. J. Heat Mass Transfer 49 (2006) 669–682.
[27] M.K. Sung, I. Mudawar, Correlation of critical heat flux in hybrid jet impingement/micro-channel cooling scheme, Int. J. Heat Mass Transfer 49 (2006) 2663–2672.
[28] M.K. Sung, I. Mudawar, Low temperature hybrid micro-channel/micro-jet impingement cooling – selection of cooling geometry and correlation of single-phase data, Int. J. Heat Mass Transfer, in press.
[29] M.K. Sung, I. Mudawar, Single-phase and two-phase heat transfer characteristics of low temperature hybrid micro-channel/micro-jet impingement cooling, Int. J. Heat Mass Transfer, in press.
[30] Fluent 6.2.16 User's Guide, Fluent Inc., Lebanon, NH, 2005.
[31] Gambit 2.2.30 User's Guide, Fluent Inc., Lebanon, NH, 2006.
[32] B.E. Launder, D.B. Spalding, The numerical computation of turbulent flows, Comput. Meth. Appl. Mech. Eng. 3 (1974) 269–289.
[33] S.V. Patankar, Numerical Heat Transfer and Fluid Flow, Hemisphere, Washington, DC, 1980.